Supplementary Information

Triggering Reversible Anion Redox Chemistry in O3-Type Cathode through Tuning Na/Mn Anti-Site Defects

Yang Yu[a,b,‡], Jicheng Zhang[a,‡], Rui Gao[a], Deniz Wong[c], Ke An[d], Lirong Zheng[e], Nian Zhang[f], Christian Schulz[c], and Xiangfeng Liu[a,b,*]

[a] Center of Materials Science and Optoelectronics Engineering, College of Materials Science and Optoelectronic Technology, University of Chinese Academy of Sciences, Beijing 100049, P. R. China

[b] College of Sino-Danish, University of Chinese Academy of Sciences, Beijing 100049, P. R. China

[c] Department of Dynamics and Transport in Quantum Materials, Helmholtz-Zentrum Berlin für Materialien und Energie, Hahn-Meitner-Platz 1, Berlin, Germany

[d] Neutron Scattering Division, Oak Ridge National Laboratory, Oak Ridge, TN 37830, USA.

[e] Beijing Synchrotron Radiation Facility, Institute of High Energy Physics, Chinese Academy of Sciences, Beijing 100049, China

[f] Shanghai Institute of Microsystem and Information Technology, Chinese Academy of Sciences, Shanghai 200050, P. R. China

* Corresponding Author: E-mail: liuxf@ucas.ac.cn (X. L.)

‡ The two authors contribute to this work equally.

Table S1. The ICP data of MFN and MFNH1 cathode materials.

Materials	Measured atomic				
	Na	Mn	Fe	Ni	Ho
MFN	0.960114	0.323648	0.325001	0.351351	0.000000
MFNH0	0.955553	0.324828	0.322108	0.348292	0.004772
MFNH1	0.953917	0.322835	0.315607	0.352302	0.009255
MFNH2	0.951765	0.328028	0.306653	0.347052	0.018267

Table S2. The refined results of NPD.

Parameter	MFN	MFNH0	MFNH1	MFNH2
***a* (Å)**	2.984205(32)	2.984700(35)	2.985169(32)	2.984247(30)
***c* (Å)**	16.00020(20)	15.99840(30)	15.99765(28)	15.98964(28)
***V* (Å)**	123.3990(30)	123.4070(30)	123.4620(30)	123.4220(30)
Na-O (Å)	2.3611(4)	2.3610(4)	2.3608(4)	2.3605(4)
O-O (Å)	2.7194(7)	2.7200(7)	2.7211(7)	2.7185(7)
TM-O (Å)	2.01884(34)	2.01907(34)	2.01968(31)	2.01841(34)
TM-TM (Å)	2.98421(30)	2.98470(34)	2.98517(30)	2.98425(30)
∠O-TM-O (°)	84.65(3)	84.69(3)	84.70(3)	84.66 (3)
R_{wp} (%)	4.57	4.44	4.03	4.15
R_p (%)	3.00	3.00	2.82	2.84

Table S3. Atoms with occupancy of MFN from NPD Rietveld refinement.

Atom	Site	x	y	z	Occ	Uiso
Na	3a	0.00000	0.00000	0.00000	0.96011	0.01233
Mn1	3a	0.00000	0.00000	0.00000	0.01304	0.01233
Mn2	3b	0.00000	0.00000	0.50000	0.31061	0.00975
Fe	3b	0.00000	0.00000	0.50000	0.32500	0.00975
Ni	3b	0.00000	0.00000	0.50000	0.35135	0.00975
Ho	3b	0.00000	0.00000	0.50000	0.00000	0.00000
O	6c	0.00000	0.00000	0.23243	0.98937	0.01288

Table S4. Atoms with occupancy of MFNH0 from NPD Rietveld refinement.

Atom	Site	x	y	z	Occ	Uiso
Na	3a	0.00000	0.00000	0.00000	0.95555	0.01186
Mn1	3a	0.00000	0.00000	0.00000	0.01752	0.01186
Mn2	3b	0.00000	0.00000	0.50000	0.30731	0.00978
Fe	3b	0.00000	0.00000	0.50000	0.32211	0.00978
Ni	3b	0.00000	0.00000	0.50000	0.34829	0.00978
Ho	3b	0.00000	0.00000	0.50000	0.00477	0.00978
O	6c	0.00000	0.00000	0.23244	0.98313	0.01319

Table S5. Atoms with occupancy of MFNH1 from NPD Rietveld refinement.

Atom	Site	x	y	z	Occ	Uiso
Na	3a	0.00000	0.00000	0.00000	0.95392	0.01196
Mn1	3a	0.00000	0.00000	0.00000	0.02016	0.01196
Mn2	3b	0.00000	0.00000	0.50000	0.30268	0.01004
Fe	3b	0.00000	0.00000	0.50000	0.31561	0.01004
Ni	3b	0.00000	0.00000	0.50000	0.35230	0.01004
Ho	3b	0.00000	0.00000	0.50000	0.00926	0.01004
O	6c	0.00000	0.00000	0.23249	0.97692	0.01299

Table S6. Atoms with occupancy of MFNH2 from NPD Rietveld refinement.

Atom	Site	x	y	z	Occ	Uiso
Na	3a	0.00000	0.00000	0.00000	0.95177	0.01190
Mn1	3a	0.00000	0.00000	0.00000	0.02171	0.01190
Mn2	3b	0.00000	0.00000	0.50000	0.30632	0.01082
Fe	3b	0.00000	0.00000	0.50000	0.30665	0.01082
Ni	3b	0.00000	0.00000	0.50000	0.34705	0.01082
Ho	3b	0.00000	0.00000	0.50000	0.01827	0.01082
O	6c	0.00000	0.00000	0.23242	0.97287	0.01287

Table S7. The refined results of XRD.

	MFN	MFNH0	MFNH1	MFNH2
***a* (Å)**	2.97831(11)	2.97977(10)	2.98111(16)	2.97988(11)
***c* (Å)**	16.0432(7)	16.0381(7)	16.0283(10)	16.0397(7)
***V* (Å)**	123.243(9)	123.325(8)	123.360(12)	123.346(9)
R_{wp} (%)	3.07	3.97	3.91	5.17
R_p (%)	2.34	2.86	2.87	3.70

Table S8. The lattice parameters of the MFN and MFNH1 cathode materials after 200 cycles, in the voltage range of 1.5-4.3 V, at the cycling rate of 0.1 C.

	MFN	MFN 200cycle	Δ(%)	MFNH1	MFNH1 200cycle	Δ(%)
***a* (Å)**	2.9783	2.9681	0.34	2.9811	2.9761	0.16
***c* (Å)**	16.0432	15.9329	0.69	16.0283	15.9818	0.29
***V* (Å^3)**	123.24	121.56	1.36	123.36	122.59	0.62

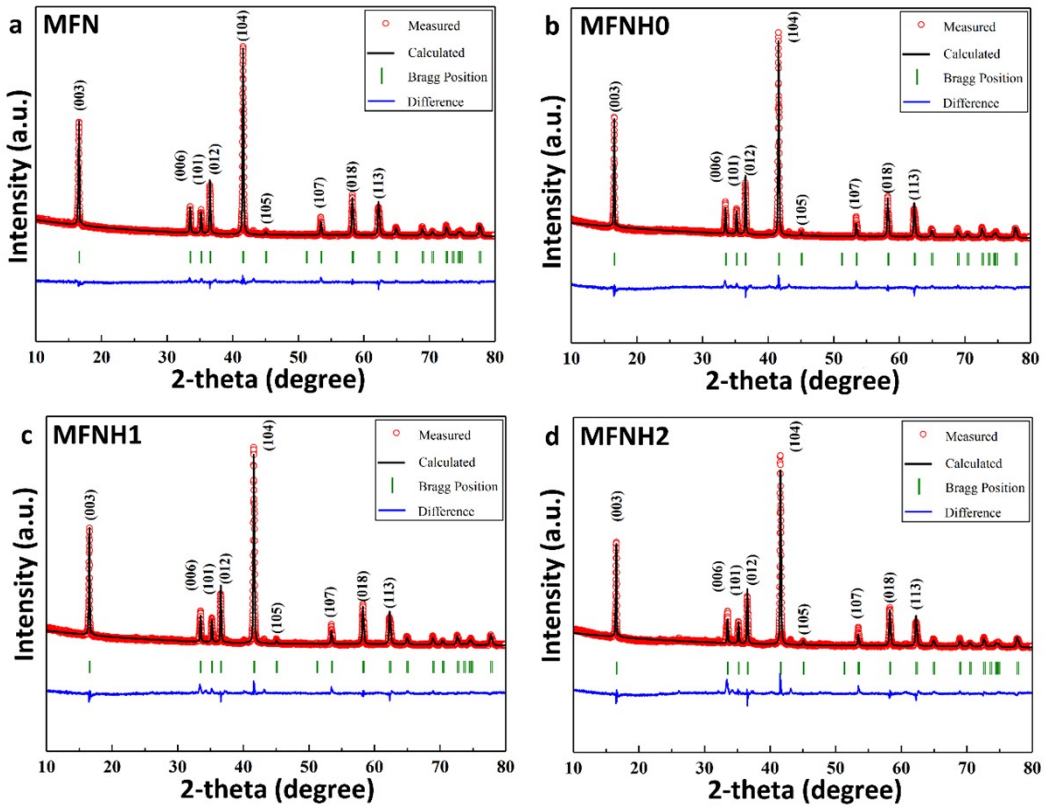

Figure S1. XRD refinement diagram of (a) MFN, (b) MFNH0, (c) MFNH1, (d) MFNH2.

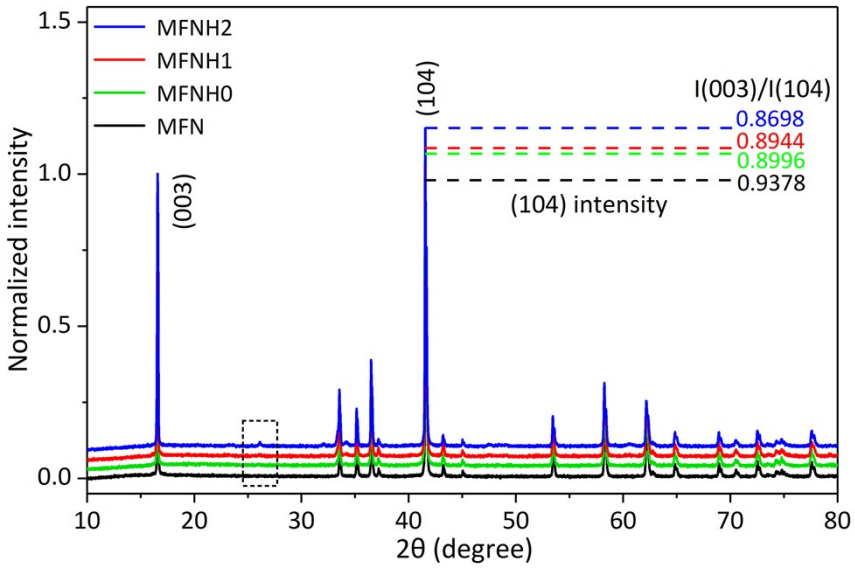

Figure S2. Normalized (003)/(104) peak intensity ratio diagram of MFN, MFNH0, MFNH1, MFNH2.

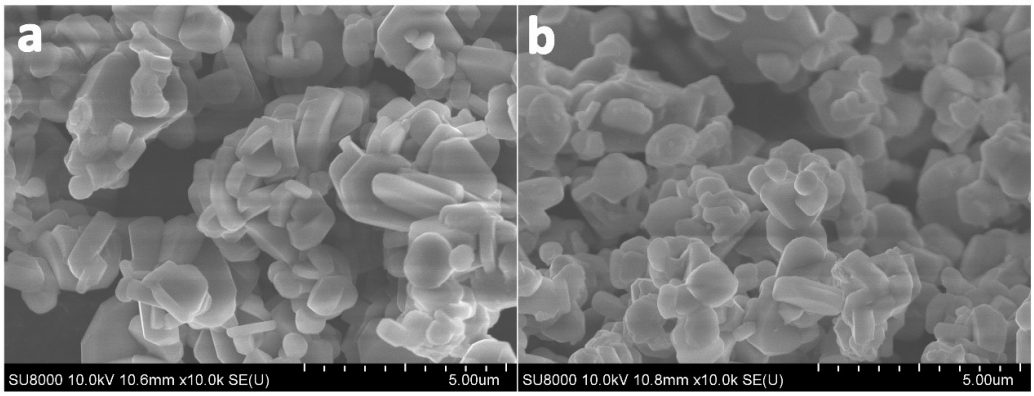

Figure S3. The SEM images of (a) MFN and (b) MFNH1.

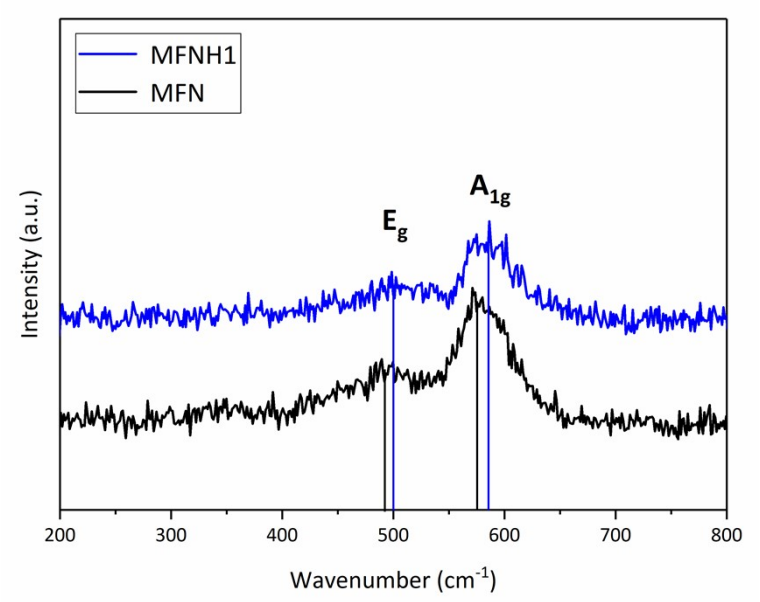

Figure S4. The Raman spectra results of MFN and MFNH1.

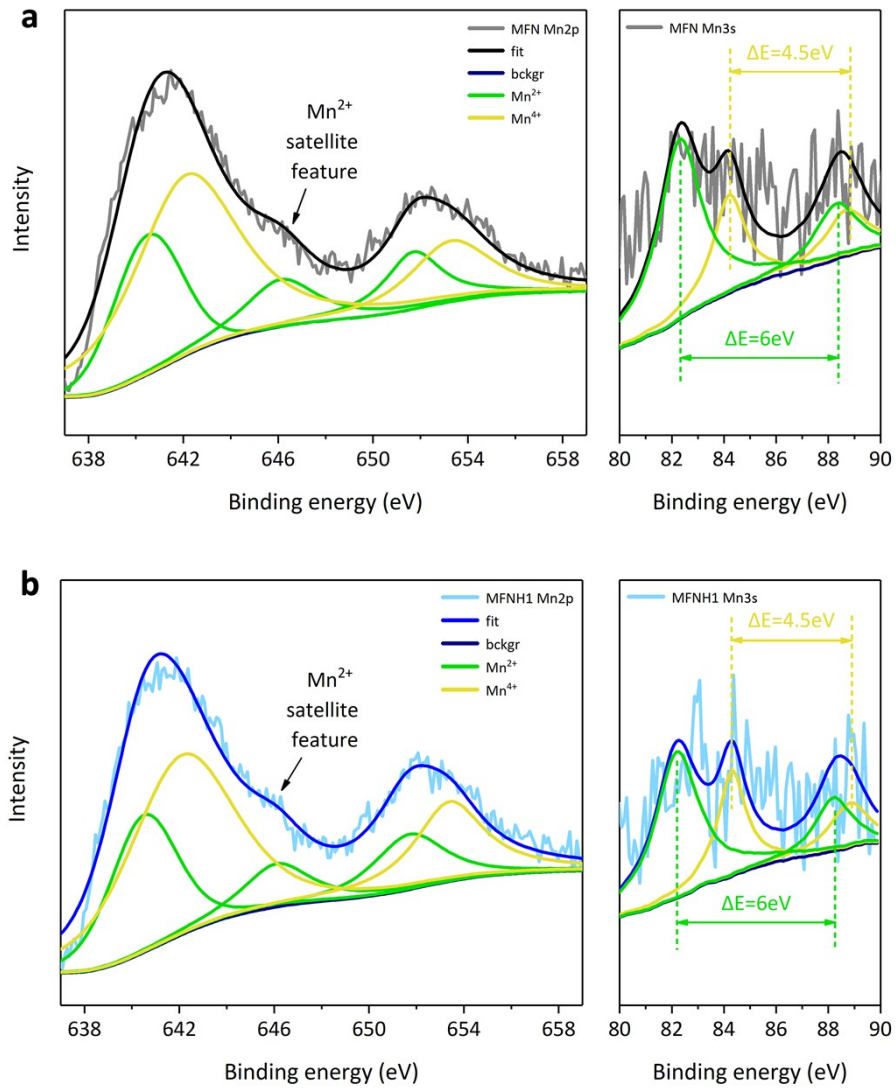

Figure S5. The XPS results of Mn 2*p* and 3*s* orbits results of the powder of (a) MFN and (b) MFNH1, etched to 15 nm.

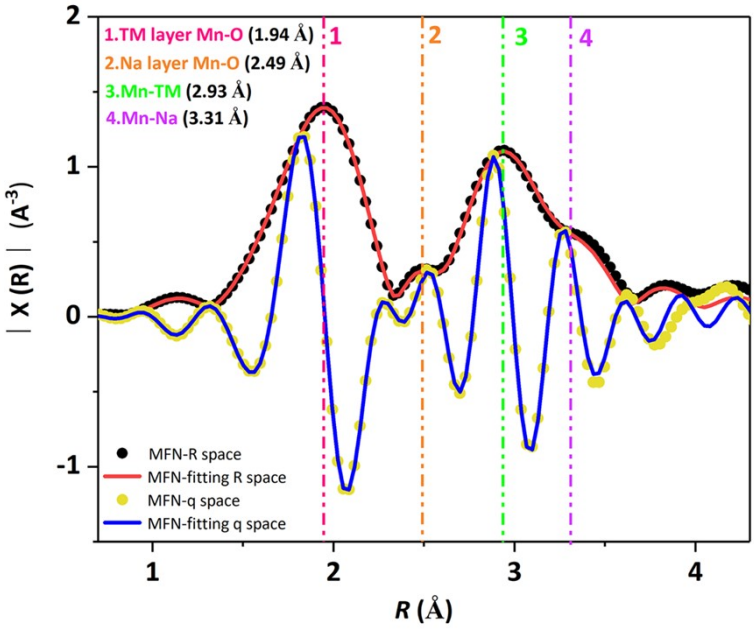

Figure S6. The R-space and q-space fitting results of MFN.

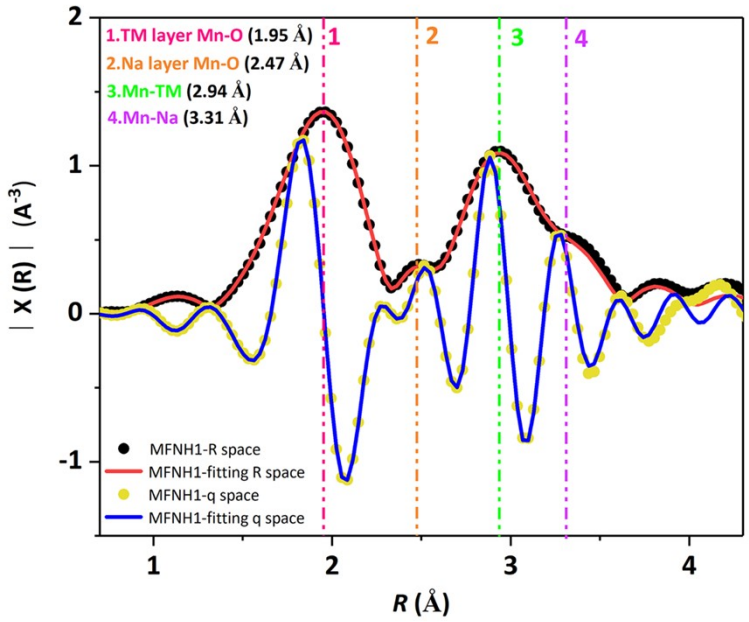

Figure S7. The R-space and q-space fitting results of MFNH1.

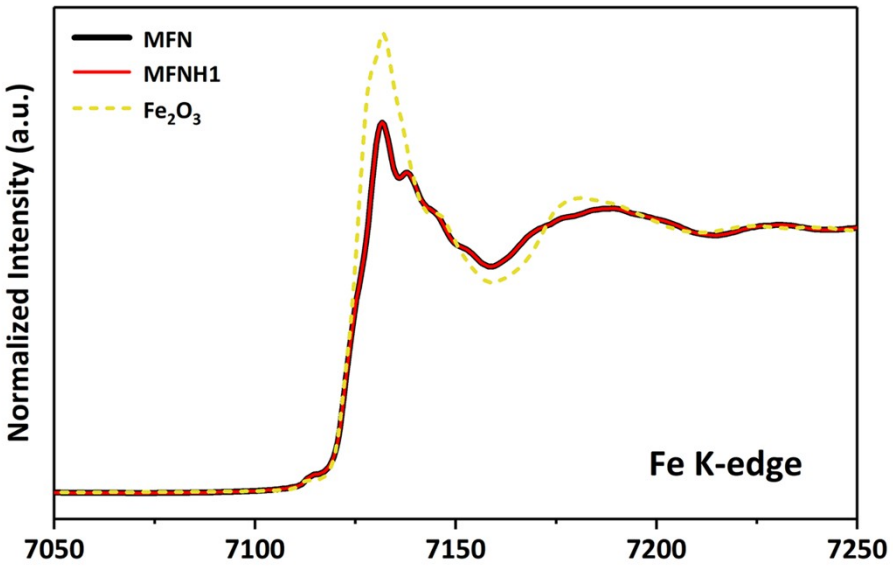

Figure S8. XANES spectra at Fe K-edge of MFN and MFNH1.

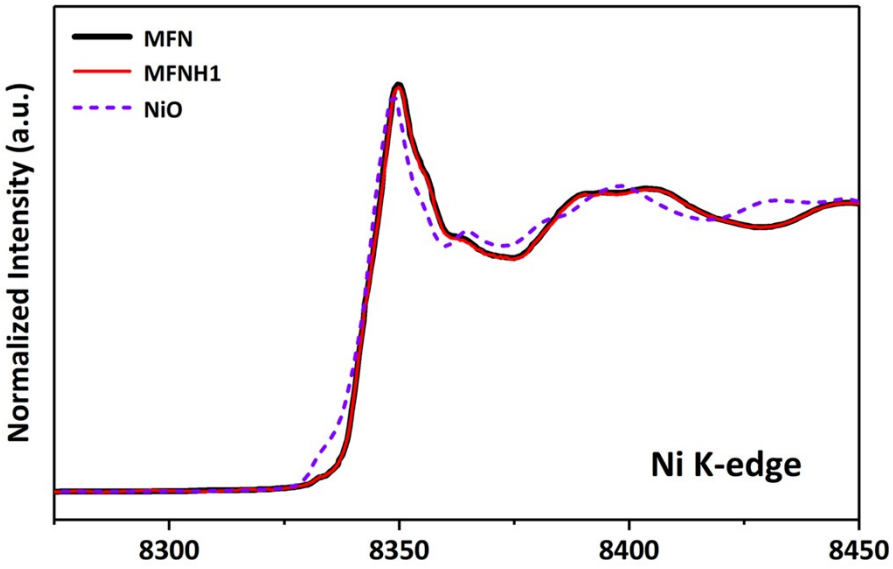

Figure S9. XANES spectra at Ni K-edge of MFN and MFNH1.

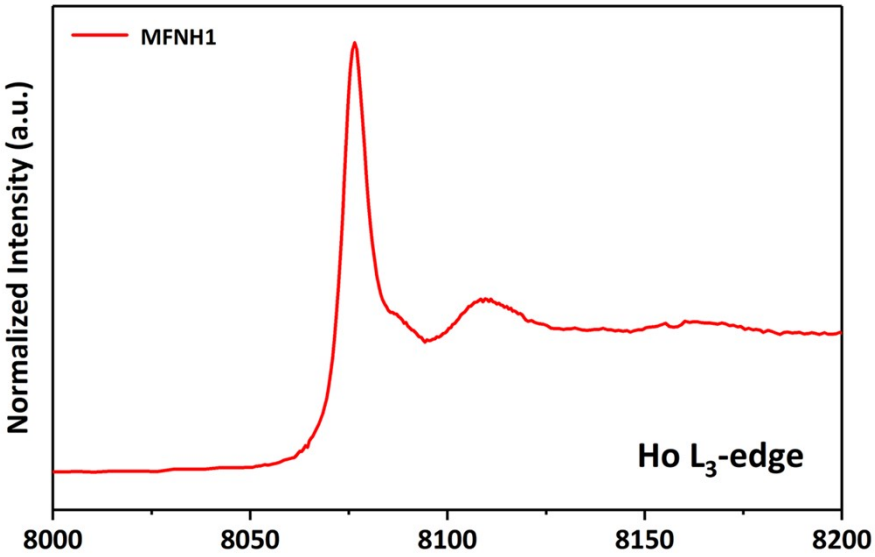

Figure S10. XANES spectra at Ho L_3-edge of MFNH1.

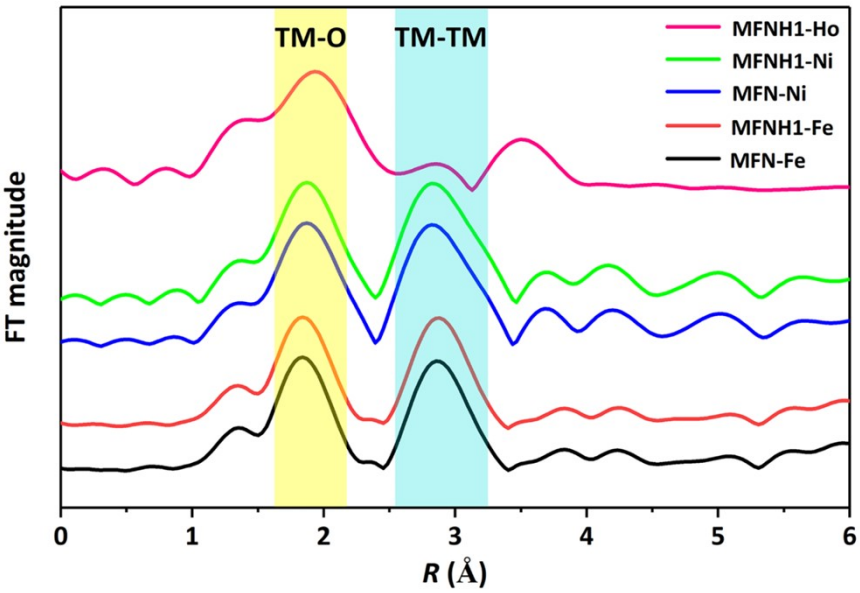

Figure S11. R-space transformation of EXAFS spectra of Fe K-edge, Ni K-edge, and Ho L_3-edge for MFN or MFNH1.

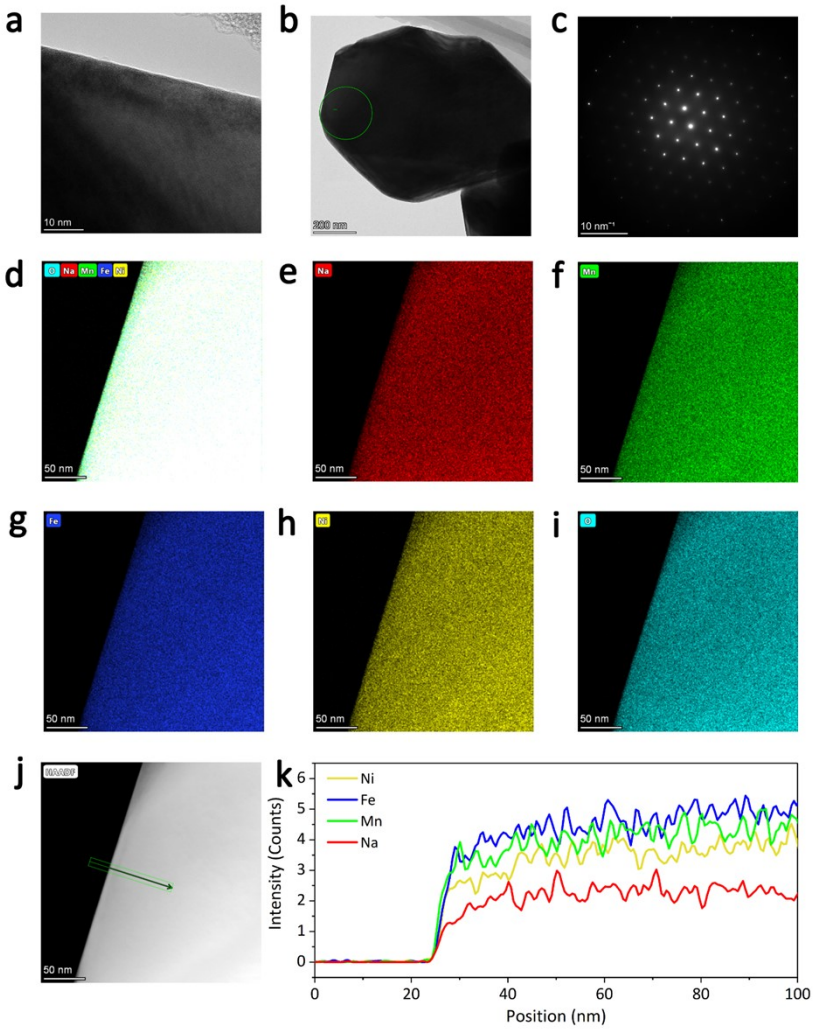

Figure S12. (a) The HR-TEM of MFN. (b) The TEM topography of MFN. (c) The SAED image of MFN, the selected area is the green circle in (b), the zone axis is [001]. (d)-(i) The TEM-EDS mapping of MFN. Detection elements include Na, Mn, Fe, Ni, O. (j) Area map of line scanning. (k) Elemental line scan results of Na, Mn, Fe, and Ni for MFN.

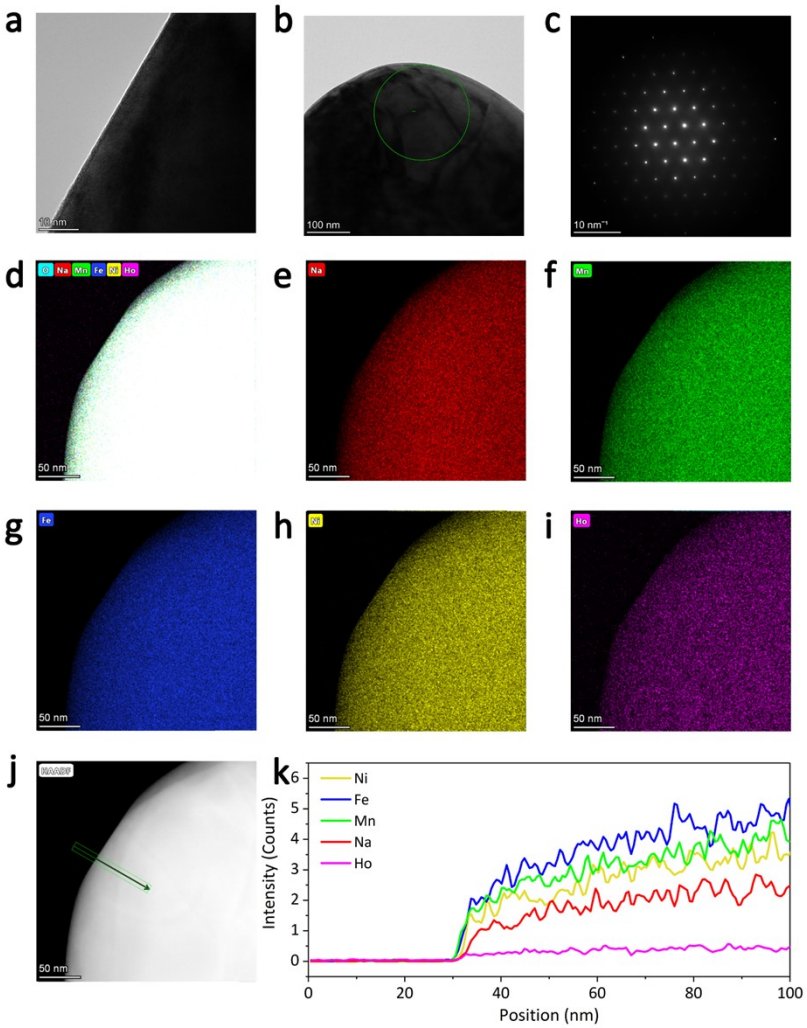

Figure S13. (a) The HR-TEM of MFNH0. (b) The TEM topography of MFNH0. (c) The SAED image of MFNH0, the selected area is the green circle in (b), the zone axis is [001]. (d)-(i) The TEM-EDS mapping of MFNH0. Detection elements include Na, Mn, Fe, Ni, Ho. (j) Area map of line scanning. (k) Elemental line scan results of Na, Mn, Fe, Ni and Ho for MFNH0.

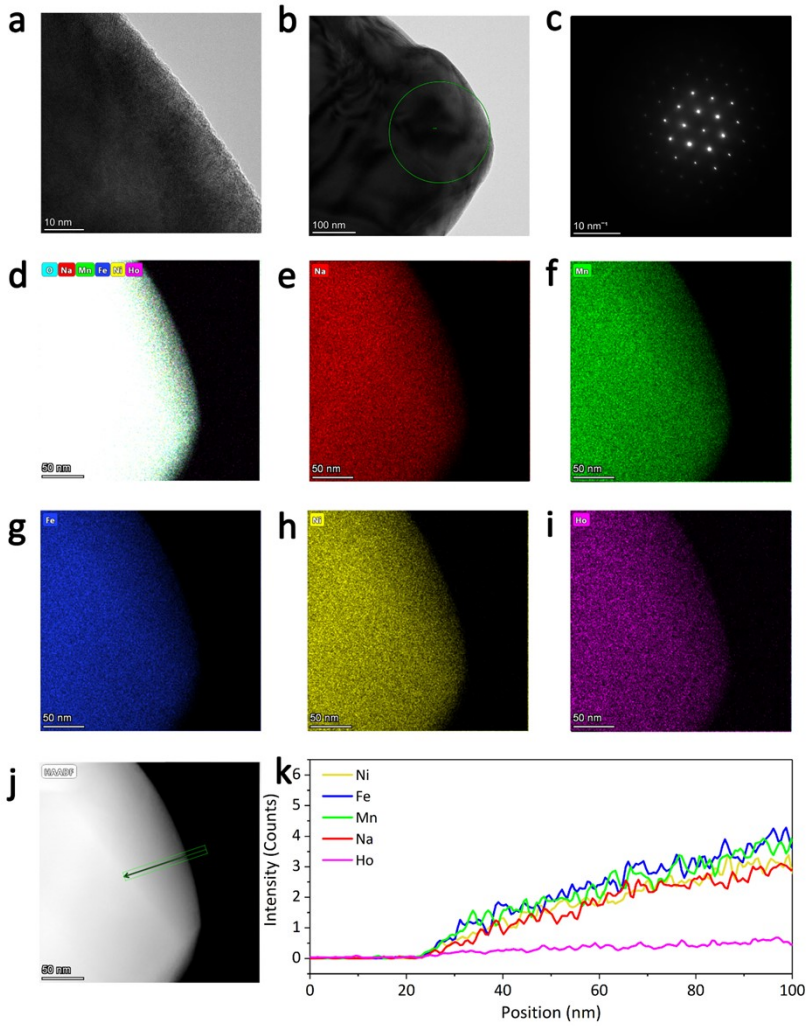

Figure S14. (a) The HR-TEM of MFNH1. (b) The TEM topography of MFNH1. (c) The SAED image of MFNH1, the selected area is the green circle in (b), the zone axis is [001]. (d)-(i) The TEM-EDS mapping of MFNH1. Detection elements include Na, Mn, Fe, Ni, Ho. (j) Area map of line scanning. (k) Elemental line scan results of Na, Mn, Fe, Ni and Ho for MFNH1.

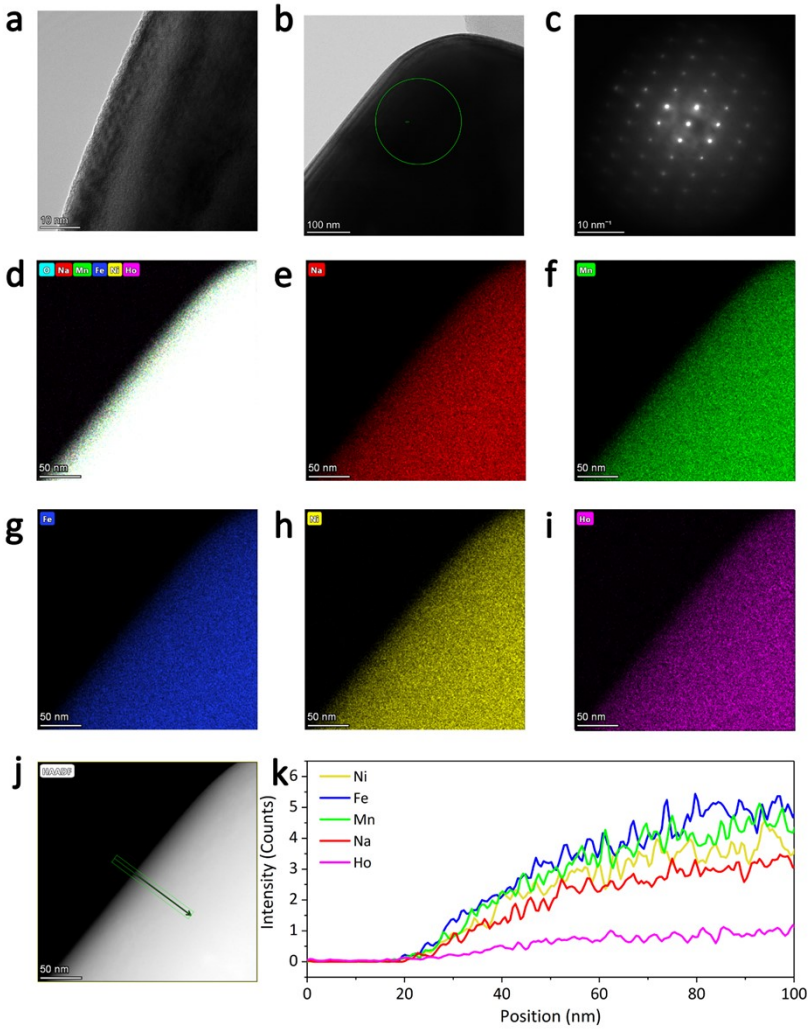

Figure S15. (a) The HR-TEM of MFNH2. (b) The TEM topography of MFNH2. (c) The SAED image of MFNH2, the selected area is the green circle in (b), the zone axis is [001]. (d)-(i) The TEM-EDS mapping of MFNH2. Detection elements include Na, Mn, Fe, Ni, Ho. (j) Area map of line scanning. (k) Elemental line scan results of Na, Mn, Fe, Ni and Ho for MFNH2.

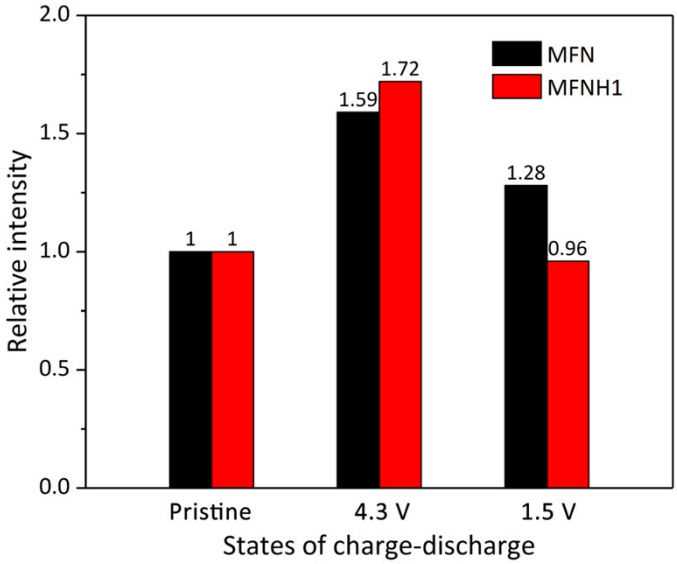

Figure S16. A comparison of the relative integrated intensity for the MFN and MFNH1 samples in the lower energy region (shaded regions).

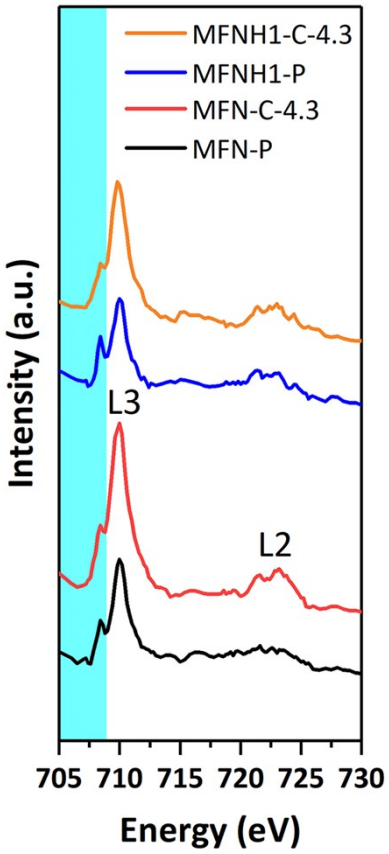

Figure S17. The Fe L-edge spectra for MFN and MFNH1 electrodes at pristine and 4.3 V charged states.

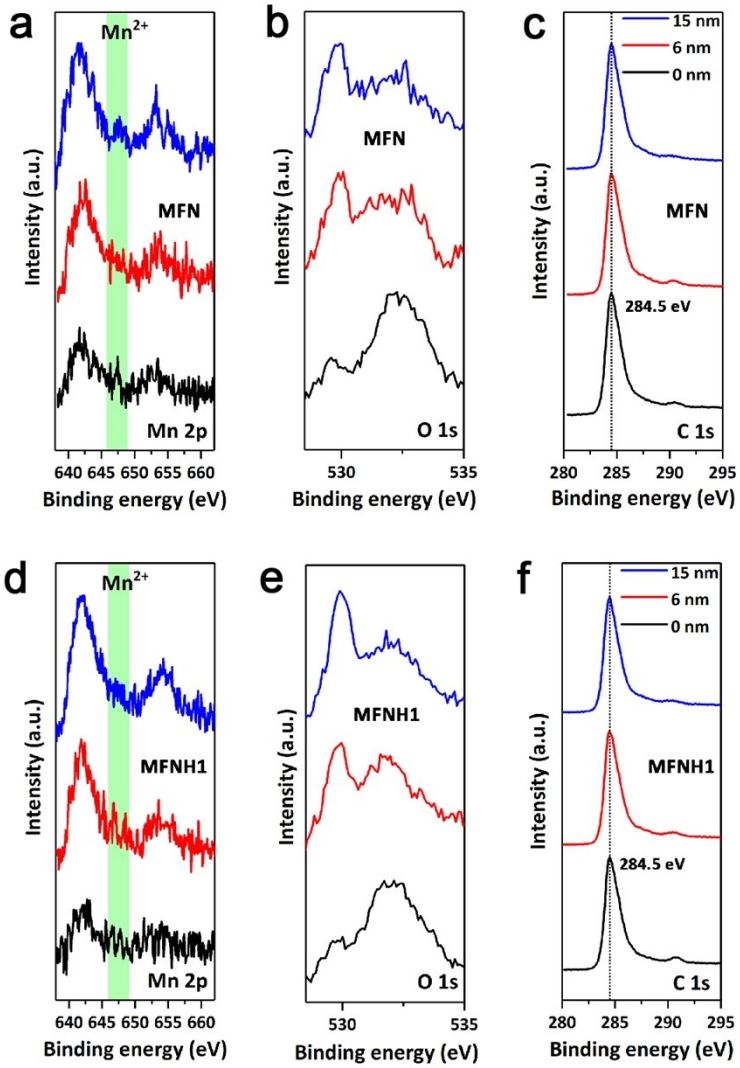

Figure S18. The surface data of (a) Mn, (b) O, (c) C XPS spectra for the pristine MFN electrodes with etching 0 nm, 6 nm, 15nm. The surface data of (d) Mn, (e) O, (f) C XPS spectra for the pristine MFNH1 electrodes with etching 0 nm, 6 nm, 15nm.

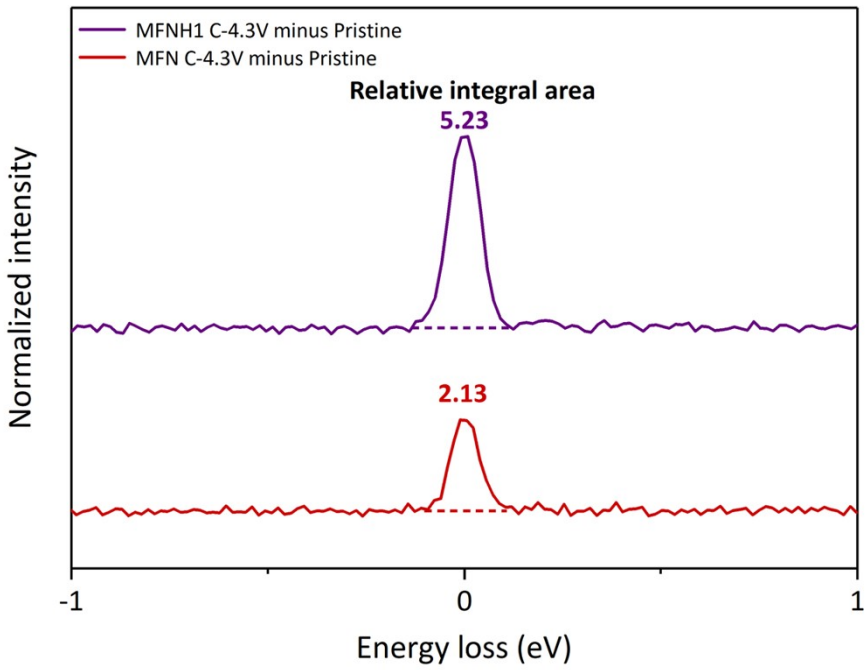

Figure S19. The integral area of the elastic peak in region A (different voltage minus pristine) of MFNH1 and MFN.

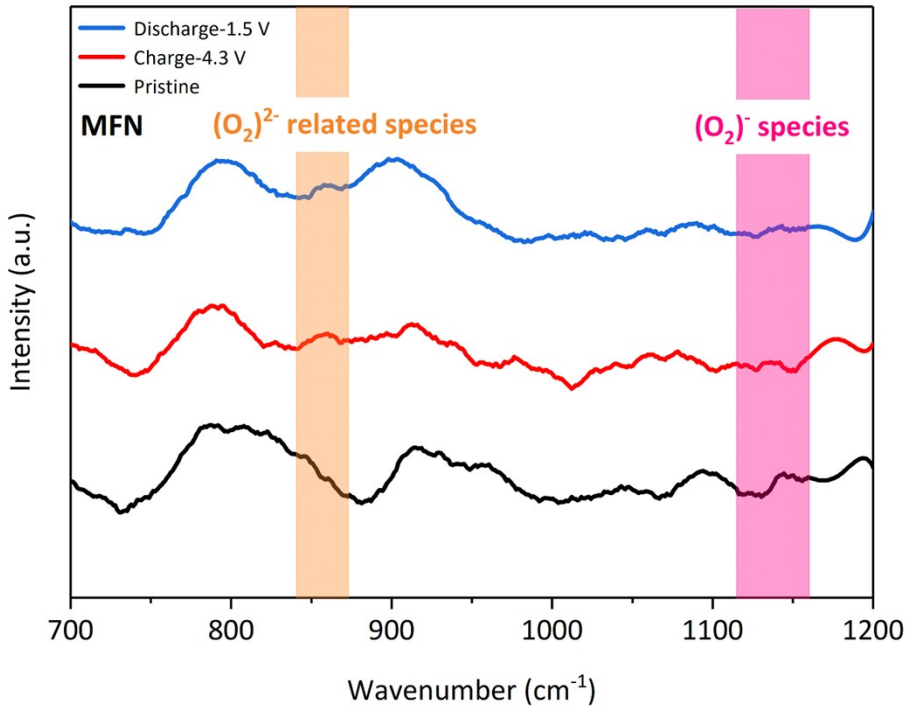

Figure S20. Ex-situ Raman spectroscopy results of MFN.

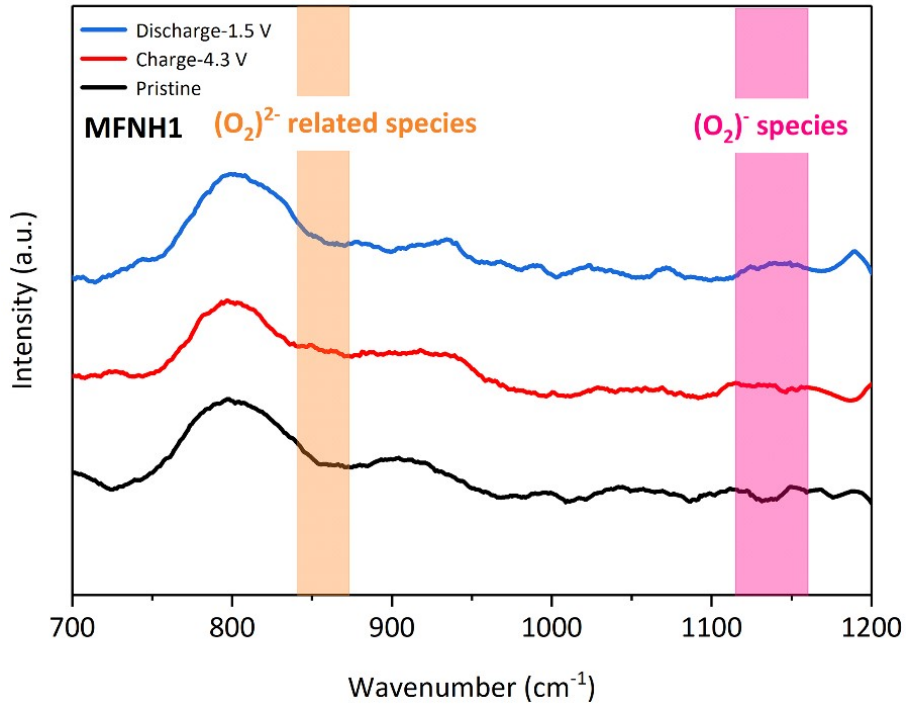

Figure S21. Ex-situ Raman spectroscopy results of MFNH1.

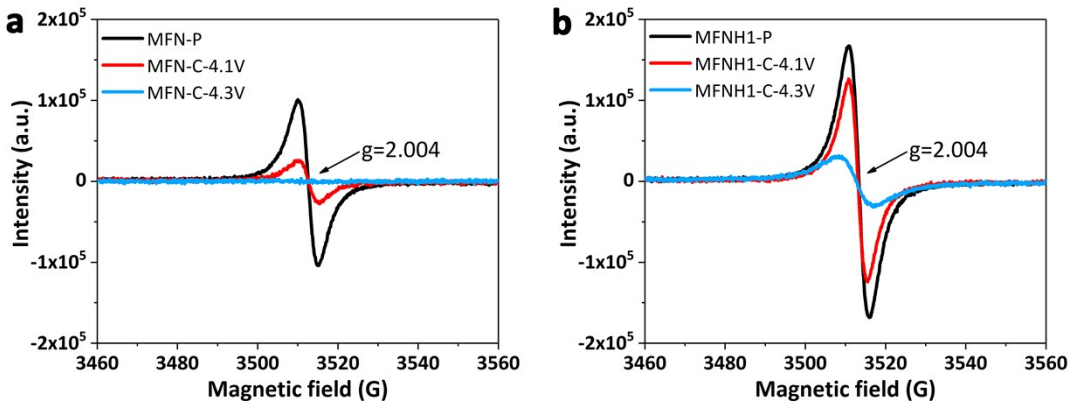

Figure S22. Ex-situ EPR results of (a) MFN and (b) MFNH1.

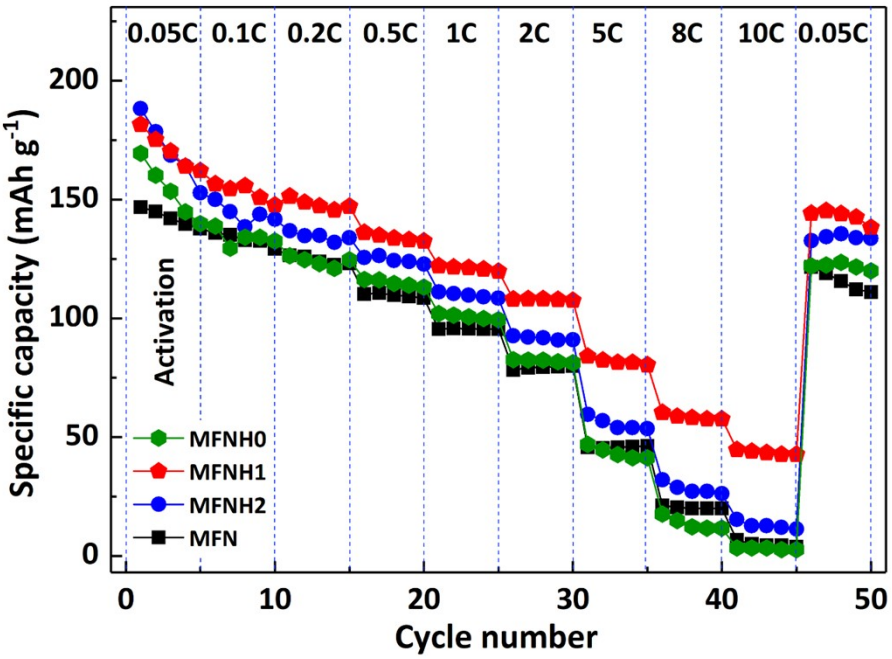

Figure S23. The rate capability of MFN, MFNH0, MFNH1 and MFNH2.

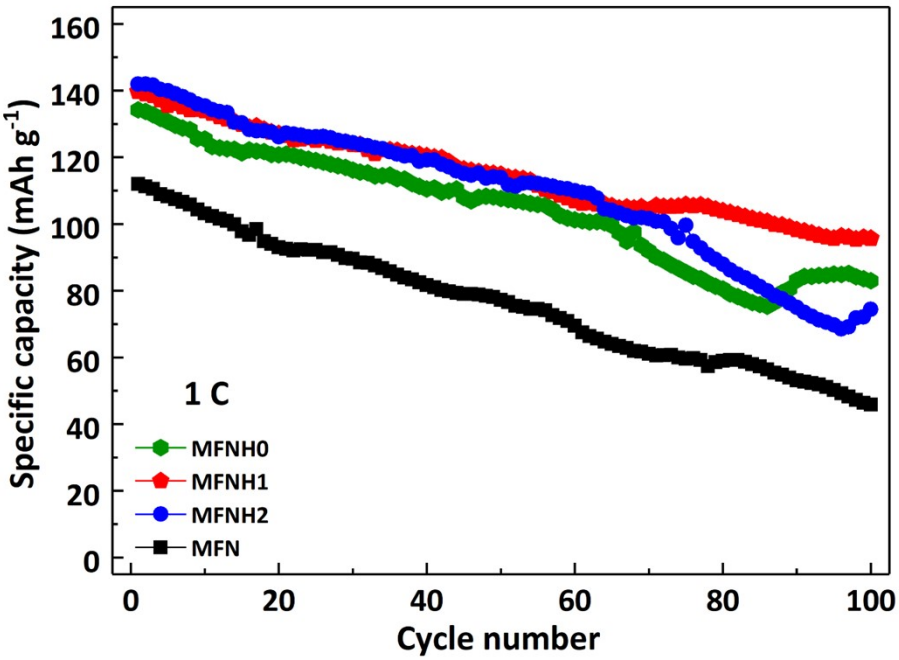

Figure S24. The cycle performance of MFN, MFNH0, MFNH1 and MFNH2 at 1 C.

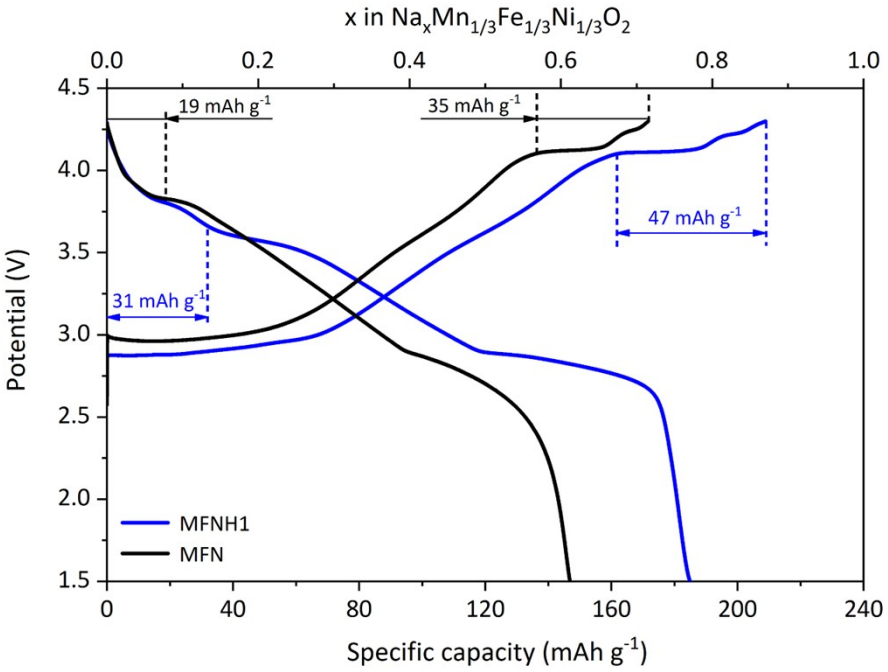

Figure S25. The first charge-discharge curves of MFN and MFNH1.

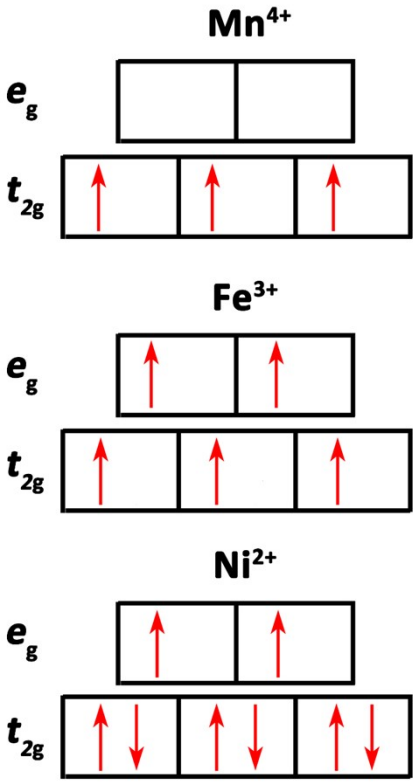

Figure S26. In MO_6, the distribution and arrangement of transition metal *d* electrons at energy levels e_g and t_{2g}.

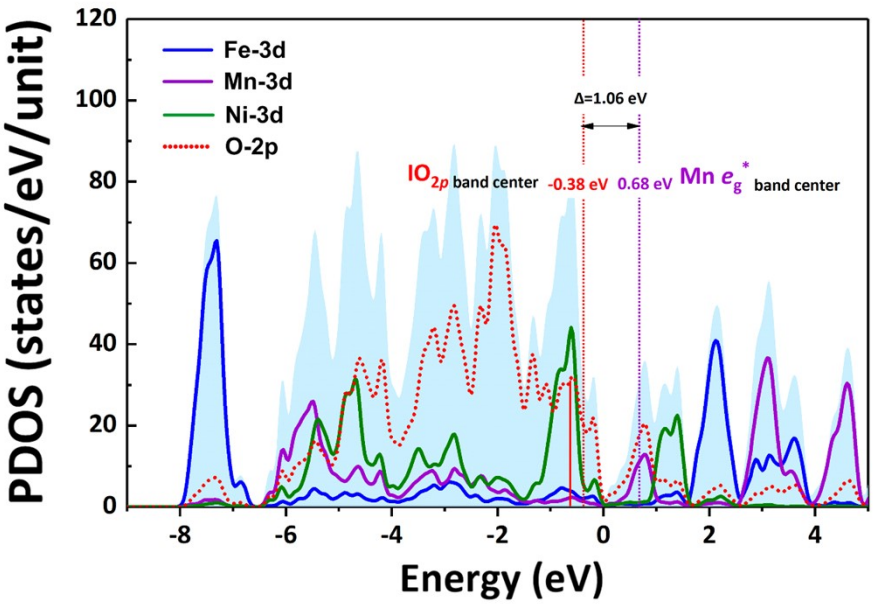

Figure S27. IO_{2p} and Mn e_g^* orbitals band center from MFN PDOS result. Band center = $(\int_A^0 E \cdot DOS \cdot dE)/(\int_A^0 DOS \cdot dE)$.

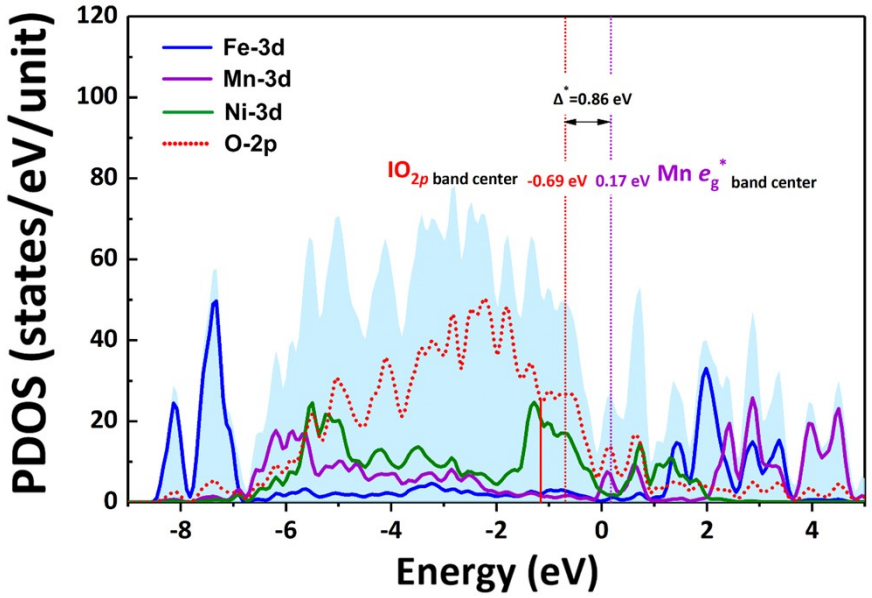

Figure S28. IO_{2p} and Mn e_g^* orbitals band center from MFNH1 PDOS result. Band center = $(\int_A^0 E \cdot DOS \cdot dE)/(\int_A^0 DOS \cdot dE)$.

Experimental Section

Synthesis of Cathode Materials

The compound $NaMn_{1/3}Fe_{1/3}Ni_{1/3}O_2$ (MFN) has been synthesized by a simple solid-state method. In this way, fully mix a certain stoichiometric ratio of Na_2CO_3 (3% excess), MnO, Fe_2O_3, and NiO powder with ball-milling machine. After full milling for 10 hours, the powder was taken out and calcined at 900 °C for 12 hours in air.

The compound $NaMn_{1/3}Fe_{1/3-x}Ni_{1/3}Ho_xO_2$ (MFNH*x*) has been synthesized by solid-state method. Fully mix a certain stoichiometric ratio of Na_2CO_3 (3% excess), MnO, Fe_2O_3, and NiO, Ho_2O_3 (the amount of Ho_2O_3 in three groups of samples were 0.5 wt%, 1 wt%, 2 wt%, respectively) powder with ball-milling machine. After full milling for 10 hours, the powder was taken out and calcined at 900 °C for 12 hours in air. The product of MFNH*x* active material was obtained.

Material Characterization and Analysis

The neutron powder diffraction (NPD) data were obtained on the VULCAN beamline at the Spallation Neutron Sources (SNS) in the Oak Ridge National Laboratory, the incident beam had the size of 5 mm×12 mm, and 5 mm receiving collimators, the bandwidth of the incident beam was 0.7-3.5 Å, and it was selected by employing the double-disk choppers at a speed of 30 Hz, 0.5-2.5 Å *d*-space was allowed in the diffracted patterns in the θ ± 90° detector banks. The $\Delta d/d$ was around 0.25% at the high-resolution mode. The power of SNS was at nominal 1400 kW, and the NPD data collection took up to three hours at the temperature of 25 ℃, the

VDRIVE software was used to reduce the data. Full-pattern Rietveld refinement was carried out using the GSAS programs with the EXPGUI interface.

The X-ray diffraction (XRD) patterns of samples were collected on the X-ray diffractometer (Cu Kα, λ= 1.5406 Å, 2-theta range = 10-70°, step width = 0.01°, scan rate = 10°/min, 45 kV, 200 mA, Rigaku SmartLab).

Hard X-ray absorption spectroscopy (XAS) were collected on the 1W1B beamline of the Beijing Synchrotron Radiation Facility (BSRF). Soft X-ray absorption spectroscopy data was collected at BL02B02 in Shanghai Synchrotron Radiation Center (SSRF). For ex-situ XAS, ex-situ XRD analysis, the cathodes were collected from dismantled cells and washed thoroughly with dimethyl carbonate (DMC).

Ex-situ O K-edge resonant inelastic X-ray scattering (RIXS) data of the electrodes was collected at the PEAXIS beamline of synchrotron BESSY II at Helmholtz-Zentrum Berlin (HZB) at an excitation energy of 531.0 eV[1].

The element compositions and valence states of materials were collected by an X-ray photoelectronic spectrometer (XPS, AXIS Supra by Kratos Analytical with an Al Kα X-ray source, 1486.8 eV).

Raman results were characterized by an inVia microscope confocal Raman spectrometer of Renishaw, UK, with a laser wavelength of 532 nm.

Scanning transmission electron microscope (STEM) experiment used by Cs-corrected (S) TEM (FEI Titan Cubed Themis G2 300).

Field emission transmission electron microscopy (TEM, Tecnai G2 F20 S-

TWIN, 200 kV) and field emission scanning electron microscopy (FE-SEM, Hitachi SU8010) were applied to observe the microstructure.

The OmniStar GSD 320 instrument with QMA 200M analyzer and C-SEM/Faraday detector was used to collect the differential electrochemical mass spectrometry (DEMS) spectra.

Electron paramagnetic resonance spectroscopy (EPR) experiment used by Bruker A300-10/12.

Electrochemical Measurements

Active material, super P carbon and poly (1, 1-difluoroethylene) (PVDF were evenly mixed and coated on aluminum foil at a ratio of 75:15:10 to form cathode material with solvent N-methyl pyrrolidinone (NMP). Cells were assembled from cathode materials, sodium piece as counter electrodes, 1.0 M $NaClO_4$ in propylene carbonate as electrolyte and GF/D (Whatman) glass fiber as separator. The mass of the loaded active material is generally controlled at about 2 mg cm^{-2}. Galvanostatic charging and discharging tests were performed using an automatic galvanostat (NEWARE). Cyclic voltammetry (CV), potentiostatic intermittent titration technique (PITT) and electrochemical impedance spectroscope (EIS) were carried out on the electrochemical workstation (PGSTAT302N, Autolab).

DFT Theoretical Calculation

First-principle calculations were performed by the density functional theory (DFT) using vienna ab-initio simulation package (VASP)[2]. The generalized gradient approximation (GGA) with the Perdew-Burke-Ernzerhof (PBE) functional were used

to describe the electronic exchange and correlation effects[3]. Uniform G-centered k-points meshes with a resolution of 2π*0.04 $Å^{-1}$ and Methfessel-Paxton electronic smearing were adopted for the integration in the Brillouin zone for geometric optimization. The simulation was run with a cutoff energy of 500 eV throughout the computations. These settings ensure convergence of the total energies to within 1 meV per atom. Structure relaxation proceeded until all forces on atoms were less than 1 meV $Å^{-1}$ and the total stress tensor was within 0.01 GPa of the target value. To describe the on-site Coulomb interaction, the Hubbard U correction (GGA+U) was applied to the transition metals. The value of Ueff (U-J) was set to 5 eV for 3*d* TM elements[4]. In order to clarify the bonding and antibonding properties of Mn-O, Ni-O, Fe-O and Ho-O, we calculated the COOP by LOBSTER program.

Supplementary References

1. C. Schulz, K. Lieutenant, J. Xiao, T. Hofmann, D. Wong and K. Habicht, *Journal of Synchrotron Radiation*, 2020, **27**, 238-249.
2. G. Kresse and J. Furthmüller, *Computational Materials Science*, 1996, **6**, 15-50.
3. J. P. Perdew, K. Burke and M. Ernzerhof, *Physical Review Letters*, 1996, **77**, 3865-3868.
4. M. H. N. Assadi and Y. Shigeta, *RSC Advances*, 2018, **8**, 13842-13849.